Journal of
Biomedical Optics

BiomedicalOptics.SPIEDigitalLibrary.org

High-speed polarization imaging of dynamic collagen fiber realignment in tendon-to-bone insertion region

Xianyu Wu
Mark Pankow
Hsiao-Ying Shadow Huang
Kara Peters

SPIE.

Xianyu Wu, Mark Pankow, Hsiao-Ying Shadow Huang, Kara Peters, "High-speed polarization imaging of dynamic collagen fiber realignment in tendon-to-bone insertion region," *J. Biomed. Opt.* **23**(11), 116002 (2018), doi: 10.1117/1.JBO.23.11.116002.

Journal of Biomedical Optics 23(11), 116002 (November 2018)

High-speed polarization imaging of dynamic collagen fiber realignment in tendon-to-bone insertion region

Xianyu Wu,[a] Mark Pankow,[a] Hsiao-Ying Shadow Huang,[a] and Kara Peters[a,*]
[a]North Carolina State University, Department of Mechanical and Aerospace Engineering, Raleigh, North Carolina, United States

Abstract. A high-speed polarization imaging instrument is demonstrated to be capable of measuring the collagen fiber alignment orientation and alignment strength during high-displacement rate dynamic loading at acquisition rates up to 10 kHz. The implementation of a high-speed rotating quarter wave plate and high-speed camera in the imaging system allows a minimum measurement acquisition time of 6 ms. Sliced tendon-to-bone insertion samples are loaded using a modified drop tower with an average maximum displacement rate of 1.25 m/s, and imaged using a high-speed polarization imaging instrument. The generated collagen fiber alignment angle and strength maps indicate the localized deformation and fiber realignment in tendon-to-bone samples during dynamic loading. The results demonstrate a viable experimental method to monitor collagen fiber realignment in biological tissue under high-displacement rate dynamic loading. [DOI: 10.1117/1.JBO.23.11.116002]

Keywords: polarized light imaging; bioimaging; dynamic loading; biological tissue.

Paper 180333R received Jun. 7, 2018; accepted for publication Oct. 15, 2018; published online Nov. 3, 2018.

1 Introduction

Highly aligned collagenous tissues possess anisotropic and viscoelastic material properties due to their structural configuration and constituent material properties.[1,2] The presence of local collagen fiber alignment is a major contributor to the anisotropic and transversely isotropic tissue material properties. Thus the alignment orientation and alignment strength of these collagen fibers are critical parameters to measure for a better understanding of tissue behavior. At the microscale, the collagen fibers in highly aligned tissues are sinusoidally crimped.[3,4] As a tensile load is applied on the tissue, the collagen fibers first straighten and then reorient. Tissue-level stress does not occur in the fiber–fibril complex until the fiber-level crimp has been straightened.[5–7] When the applied load is further increased, the stress–strain curve undergoes a nonlinear transition with the straightened collagen fibers becoming the primary load-bearing structure.[8] Previous experimentally obtained stress–strain curves also demonstrate significant strain-rate dependence in the mechanical behavior of ligament and tendon tissue.[9–13]

Less mechanical behavior data are available on the tendon-to-bone insertion as the small size and complexity of this region make experimental characterizations difficult. The properties of this tendon-to-bone insertion region are also expected to be highly strain-rate dependent. The microstructure and composition of the tendon-to-bone insertion region are complex with a large difference in moduli between the tendon end and the bone end.[14] The uniqueness of the insertion region microstructure is the graded collagen fiber orientation between the two ends. This graded fiber orientation is required to geometrically map the unidirectional fibers at the tendon to the curved bone surface at the other end.

Chandrasekaran et al.[14] measured a three-dimensional map of the collagen fiber orientation in tendon-to-bone insertion samples, using two-dimensional fast Fourier transform image processing of microscope images. The results were verified with previous polarization microscopy images from other research groups. The tendon-to-bone insertion has a planar distribution of aligned collagen fibers, which does not vary through the thickness of the specimens. In other words, the tendon-to-bone insertion is not multilayered, which makes it ideal for polarization imaging as the properties are constant in the direction of the propagating lightwave.

In the direction of the axis between the tendon and the bone ends, the collagen fiber showed a change in the distribution of orientation angle. The mean angle for each location along the axis is the same and follows the direction of physiologic tension, however, a gradation in the distribution of the orientation angle was observed. This distribution was minimal at the tendon end and increased along the axis until the bone end. Therefore, the tendon-to-bone insertion local properties decreased in anisotropy from the tendon to the bone end of the sample. Although the fiber alignment angle does not change, there is variability in the density of the collagen fibers through the thickness of the tendon-to-bone insertion, with the highest density found at the center of the specimen. Closer to the edges of the specimen, the collagen fiber density is lower, with an increased presence of proteoglycans and cellular circularity. This will have implications for the ability of sliced tendon-to-bone insertion specimens to represent the full tendon-to-bone insertion, as is addressed in this paper.

It is likely that rapid collagen fiber realignment during dynamic loading plays a strong role in the dynamic behavior of the tendon-to-bone insertion, as supported by finite-element models of idealized insertions.[3] In these simulations, the mean orientation angle of the collagen fiber distribution was shown to have a strong effect on resulting stresses and stress concentrations. It is hypothesized that this dynamic realignment is what makes the tendon-to-bone insertion resistant to dynamic loads and reduces injury due to these loads. Further, the presence

---

*Address all correspondence to: Kara Peters, E-mail: kjpeters@ncsu.edu

of anomalous fiber realignment during loading has been demonstrated to be a good predictor of tissue injury and later tissue failure.[15,16] It is, therefore, important to study the tendon-to-bone insertion dynamic properties and its structural reorganization during medium–high strain rate loading.

For static and low-speed loading conditions, the crimping structure can be visualized using quantitative polarized light microscopy (QPLM).[17] For high-speed dynamic events, imaging of the collagen fiber alignment angle is challenging due to the need to synchronize polarization images at high speed and the noise present in images collected from a highly scattering medium at small exposure times. Extending the QPLM method to low-speed dynamic imaging has been demonstrated either by rotating the polarizing elements at higher rotation rates or dividing the available pixels into 2×2 subregions with different polarizing elements in front of each. The first approach permits the full spatial resolution of the camera to be used, however, reduces the time resolution since multiple polarization states must be collected for each alignment angle image.[8,18,19] Wu et al.[19] were recently able to demonstrate QPLM alignment angle and retardation images of a transparent, polycarbonate specimen at 10 kHz with a 1024×1024 pixel resolution using this approach. The second approach maintains the maximum temporal resolution, however, reduces the spatial resolution and requires complex fabrication techniques for the array of polarizer elements.[20,21]

To enable the study of the tendon-to-bone insertion dynamic properties and its structural reorganization during medium–high strain rate loading, this paper adapts the high-speed QPLM technique and the drop-tower loading arrangement previously demonstrated by Wu et al.[19] Due to the small size of the tendon-to-bone insertion region, this approach was chosen because of its high spatial resolution. In particular, we study the performance of the high-speed QPLM imaging system under high light scattering and short camera exposure time conditions. Porcine digital tendon-to-bone insertion specimens were tested at medium–high loading rates and the collagen fiber realignment was monitored. As the tendon and bone ends of the tendon-to-bone insertion region have very different material properties, a special gripping mechanism was designed and implemented to permit dynamic tensile loading of the specimens. The large amount of light scattering in the tissue specimen created challenges in reaching sufficient light intensity through the specimen, which was addressed through modifying the input light source and optical components, as well as microtome slicing of tendon-to-bone insertion samples. Tendon-to-bone insertion samples of different thicknesses were also tested to investigate the trade-off between increasing the transparency of the specimen and potentially altering the mechanical behavior of the tendon-to-bone insertion sample.

2 Experimental Methods

This section describes the high-speed polarization microscopy system developed for these measurements, the preparation of tendon-to-bone insertion specimens, and the modifications implemented to a drop tower for dynamic tensile loading of the specimens.

2.1 *High-Speed Polarization Microscopy System*

The QPLM arrangement used in this work consists of a polarization state generator for generating elliptically polarized light at different azimuth angles and a polarization state analyzer (PSA) after the specimen for analyzing the polarization state of the light beam emerging from the specimen. The optical path is shown in Fig. 1.

A 633-nm, 20-mW HeNe red-light laser provided a linearly polarized input beam with the polarization axis in the vertical direction and polarization ratio of 500:1. The laser beam was expanded using a reverse optical fiber collimator, to increase the beam diameter to approximately that of the quarter wave plate (QWP) diameter, 12.7 mm. The polarized light then passes through a rotating QWP (WPQ05M-546, ThorLabs), which causes the light to become elliptically polarized at different angles. The elliptically polarized light beam then passes through the specimen, which is assumed to act as a linear birefringent medium with negligible scattering and spatially varying principal optical axes. Finally, the light passes through another fixed QWP (same as above) whose slow axis is at 45 deg to the vertical labeled as the fixed QWP in Fig. 1 and a linear polarizer (LPVISA050, ThorLabs) oriented in the horizontal direction.

The particular polarizer and quarter-wave plate components used in this experimental implementation were designed for green light (546 nm), rather than 633 nm of the laser output, as they were used in a previous implementation of the high-speed QPLM system by Wu et al.[19] There is, therefore, an inherent error in the calculation of the alignment angle and retardation maps due to the fact that the QWP does not produce an exact quarter wave rotation. However, this error was outweighed by the fact that the strong scattering properties of the biological specimens required a much higher input power density of the light beam than the previous transparent, polycarbonate specimens which could be achieved with this laser source. In addition, Tower and Tranquillo[22] demonstrated that the calculation errors due to this wavelength mismatch were negligible, using the same fast harmonic analysis technique applied here.

The implemented high-speed QPLM system is shown in Fig. 2. The output lightwave distribution from the PSA was acquired with a high-speed camera (Photron FASTCAM SA-X2) at 10,000 frames per second. The QWP was rotated at a constant speed of 5000 rpm by a high-speed servo motor

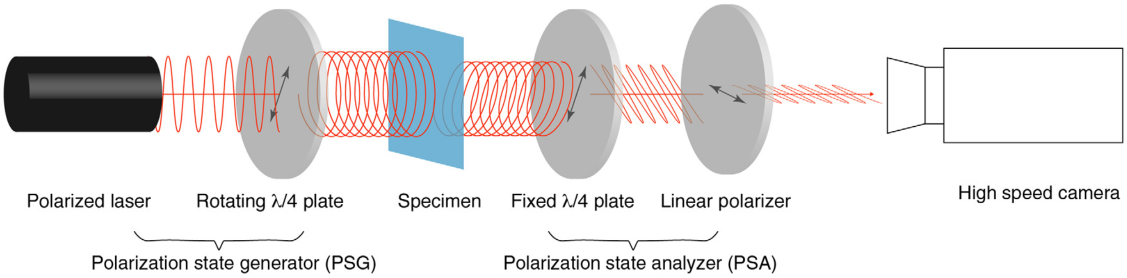

Fig. 1 Schematic of the high-speed QPLM instrument using a polarized red laser.

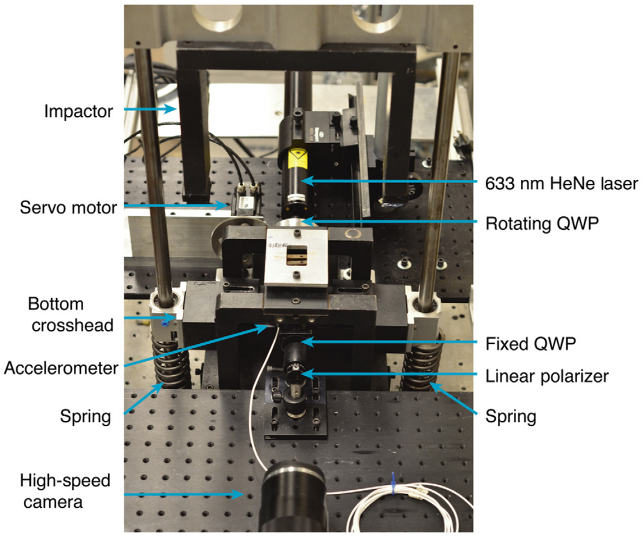

Fig. 2 Photograph of high-speed QPLM instrument and red laser setup.

(Kollmorgen AKM11B), controlled using a Kollmorgen AKD-T00306 drive with its built-in PID speed control system. The high-speed camera provides a 616×512 pixel series of images with a 12-bit resolution. The resulting spatial resolution is $\sim 100\ \mu$m per pixel. The acquired high-speed video frames were then cropped to the region of interest for analysis. The QWP rotation angle θ was synchronized with the high-speed video frames for generating alignment angle images and retardation images.[19]

The rotating QWP was rotated to 60 positions distributed evenly over 180 deg to create each alignment angle and retardation image. Based on the QWP rotation rate and camera frame rate, this was the maximum number of images available per 180-deg rotation. The calculation of the alignment angle and retardation images was based on the fast harmonic analysis method of Tower and Tranquillo.[7] Full details of the calculation method are found in Ref. 19.

For each pixel, the specimen alignment angle α_s is calculated as (applying the specific angles of the QWP in these experiments to the equations of Wu et al.[19])

$$\alpha_s = \frac{1}{2} \tan^{-1}\left[\frac{(kM_s)_{1,2}}{(kM_s)_{1,3}}\right]. \tag{1}$$

The retardation ϕ_s is determined numerically by applying the Newton Raphson algorithm to the following equation:

$$-(kM_s)_{1,4} + \frac{1}{\sqrt{2}} \cos(\phi_s) = 0. \tag{2}$$

In these equations, the four elements in the first row of the matrix kM_s are constructed from the light intensity images captured when the rotating QWP position is at the relative rotation angles, $I(\theta_i)$ $(i = 1, \dots, 60)$, as follows:

$$(kM_s)_{1,1} = \frac{1}{n} \sum_{i=1}^{n} I(\theta_i)\{1 - 2\cos[4(\theta_i + \pi/4)]\}, \tag{3}$$

$$(kM_s)_{1,2} = \frac{4}{n} \sum_{i=1}^{n} I(\theta_i) \cos[4(\theta_i + \pi/4)], \tag{4}$$

$$(kM_s)_{1,3} = \frac{4}{n} \sum_{i=1}^{n} I(\theta_i) \sin[4(\theta_i + \pi/4)], \tag{5}$$

$$(kM_s)_{1,4} = \frac{2\sqrt{2}}{n} \sum_{i=1}^{n} I(\theta_i) \sin[2(\theta_i + \pi/4)]. \tag{6}$$

Here, kM_s is normalized by the magnitude of its harmonic components:

$$\sqrt{\sum_{i=2,3,4} (kM_s)_{1,i}^2}. \tag{7}$$

Since the relative axis shift between the QWP and the axes of birefringence is periodic, the captured light intensity images from the QWP rotation from any angle x to $x + 180$ deg can be used to construct alignment angle maps and retardation maps. Therefore, n images, starting with the first image, then the second image, etc. were used to construct the alignment angle and retardation maps. The advantage of using this sequential method is that it significantly increases the imaging frequency without increasing the hardware parameters (the camera imaging frequency or the QWP rotation speed).[19]

2.2 *Specimen Preparation*

Eight digital flexor tendon-bone units were removed from porcine forelimbs procured from a local abattoir [Fig. 3(a)]. These samples were chosen because they are a relatively large tissue for imaging and easy to obtain. The raw tendon-to-bone samples were first frozen to −20°C using a cryostat. Then a microtome was used to slice 10- to 100-μm thick tendon-to-bone insertion tissue layers from the sample surface, as shown in Fig. 3(b). Prior to testing, the optimal specimen thickness was not known, so a variety of specimen thicknesses were tested. Reducing the specimen thickness improves the light intensity arriving at the high-speed camera, and therefore, increases the signal–to-noise ratio in the alignment angle and retardation images. However, reducing the specimen thickness also alters the structural geometry of the samples. This trade-off will be discussed in Sec. 3.

2.3 *Loading*

The QPLM instrument was implemented in a modified drop weight tower, as shown in Fig. 2(b), for applying controlled dynamic tensile loads to the biological specimens. Special grips were designed to clamp the tendon-to-bone insertion samples, as shown in Fig. 4. Curved, textured grips, not visible in Fig. 4 were used to clamp the tendon end of the tendon-to-bone insertion samples and were fixed to the frame of the drop tower. The bone end of the sample was held in place by the bottom crosshead. The tendon end was threaded through a hole at the center of the bottom crosshead, smaller than the size of the bone for the sample. As the bottom crosshead is displaced downward the bone end is forced downward and the tendon-to-bone insertion is loaded in tension. The displacement of the

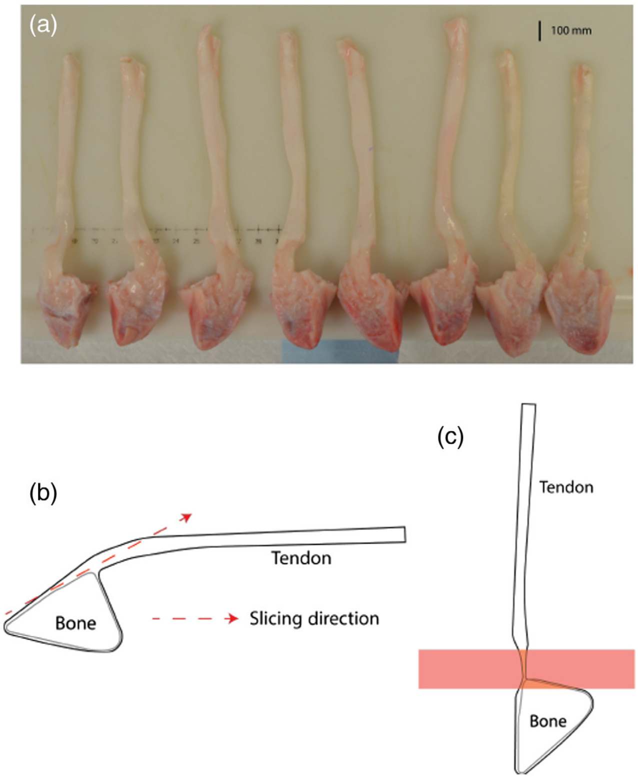

Fig. 3 (a) Photograph of raw tendon-to-bone insertion samples and schematic of (b) slicing and (c) imaging tendon-to-bone insertion samples. Path of red-light propagation through sample (from left to right) is shown in (c).

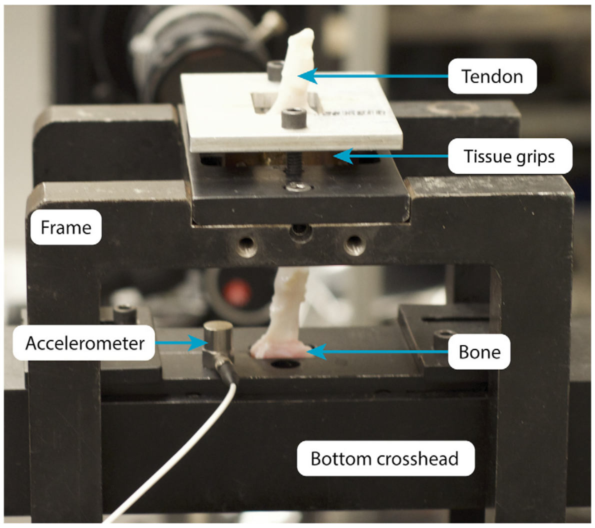

Fig. 4 Photograph of a sample mounted on the modified drop tower.

impactor is measured using a noncontact linear position sensor. The impactor was released from a height of ~180 mm.

The displacement rate of the load applied to the specimen is calculated using the force balance as a function of time t:

$$F_i(t) + F_c(t) = F_s(t), \tag{8}$$

where F_i, F_c, and F_s are the force of the indentor, the crosshead, and the two-coil springs supporting the crosshead (shown in Fig. 2), respectively. This equation neglects the mass of the specimen compared to the crosshead and impactor. The forces are calculated in terms of the measured displacement of the impactor and calculated velocity of the impactor:

$$m_i[v_i(0) - v_i(t)] + m_c[v_c(t) - v_c(0)] \\ = 2K \int_0^t [x_i(0) - x_i(t)]\mathrm{d}t, \tag{9}$$

where m_i is the mass of the impactor (10.84 kg), m_c is the mass of the crosshead (5.29 kg), and v_i and v_c are the velocities of the impactor and crosshead, respectively. Here, x_i is the displacement of the impactor, and K is the stiffness (20.458 kN/m) of each of the two springs used to decelerate the crosshead. At the start of impact, $v_i(0)$ is the freefall velocity of the impactor, which we label v_{if} and $v_c(0) = 0$, therefore

$$v_c(t) = \frac{m_i}{m_c}[v_i(t) - v_{if}] + 2\frac{K}{m_c}\int_0^t [x_i(0) - x_i(t)]\mathrm{d}t. \tag{10}$$

As the crosshead velocity and the velocity of the bone end of the tendon-to-bone insertion specimen are the same, the maximum displacement rate applied to the specimen was calculated from the maximum displacement rate of the crosshead, typically just prior to failure of the specimen.

The QWP was rotating before the crosshead was released, to ensure that it had reached a constant rotation velocity throughout the impact event. At the start the impact event, it is, therefore, necessary to identify the starting angle of the QWP. By fitting the background intensity (in the field of view but outside the specimen) to a sine wave and calculating the phase of this signal at the start of the event, the angle of the QWP for the images to be analyzed was known.

The time of initial failure was easily identifiable in the video images collected, however, the frame number at the beginning of the impact event for each specimen was less clear. As will be seen in the video images, the background light intensity outside of the specimen area fluctuated rapidly due to the rotating QWP. This effect, combined with the small specimen relative motion between video frames, made it difficult to determine the exact video frame to show the first motion of the specimen. Therefore, the trigger signal from the accelerometer was used as the consistent starting point between the different specimens. When the measured crosshead acceleration reached 490 $\mathrm{m/s^2}$ ($50g$), the oscilloscope sent a trigger to the high-speed camera and the time of the trigger signal is set to be 0 ms for all video images.

3 Experimental Results

Initial imaging was performed on a tendon-to-bone insertion specimen under static tensile loading to quantify the baseline errors in the QPLM method for a highly scattering material and high camera frame rate. Then a total of eight tendon-bone insertion specimens were prepared and tested in the modified drop tower. The specimens were ordered from thinnest (specimen 1) to thickest (specimen 8), with a mean thicknesses ranging from 0.5 to 1.5 mm. Specimen 3 slipped from the grip during loading, therefore, the data from this specimen will not be presented. The mean maximum displacement rate for all specimens was 1.25 m/s.

3.1 *QPLM Baseline Errors*

To quantify the imaging quality of the high-speed QPLM instrument for high-speed imaging of the tendon-to-bone insertion, a slight static tensile load was applied on a sliced tendon-to-bone specimen by slightly displacing the bottom crosshead to induce collagen fiber realignment. The high-speed QPLM instrument was operated using a camera frame rate of 10,000 fps and QWP rotation speed of 5000 rpm. The average recorded light intensity at a pixel in the tendon-to-bone insertion region of the unloaded specimen is plotted in Fig. 5. Since the QWP was rotating at a constant speed, the plotted average light intensity was changing sinusoidally at a constant frequency.

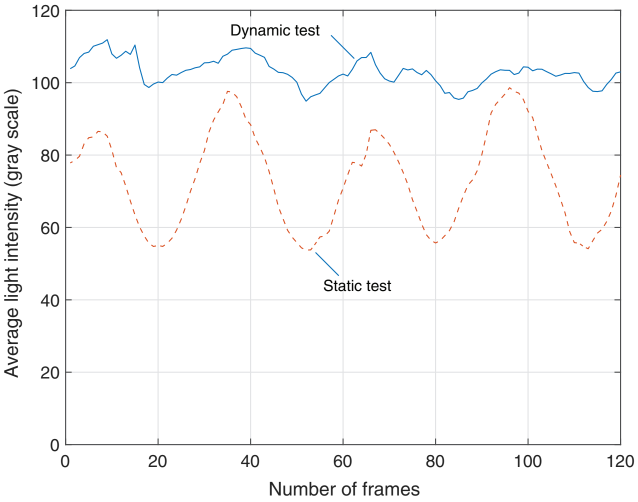

Fig. 5 Average light intensity of a pixel in the tendon-to-bone insertion region of static tensile load test specimen and dynamic load test specimen 1.

An example intensity image and the calculated alignment angle and retardation images using the 60 frames ending at this intensity image are shown in Fig. 6. Histograms of the alignment angle and retardation distributions for the region-of-interest (ROI) in the tendon-to-bone insertion are also plotted in Fig. 6. Within the tendon-to-bone insertion region, the collagen fiber alignment angle is reasonably uniform, surrounding an angle of −22 deg from the horizontal axis. The histogram of the alignment angle image is as expected, with a standard deviation of 11 deg. This variation in alignment angle is due to both the QPLM imaging system and local variations in tendon-to-bone insertion tissue. The retardation image is less uniform than the alignment, as expected since the retardation image is sensitive to local thickness variations in the tendon-to-bone insertion. The mean retardation is 74 deg, with a standard deviation of 20 deg.

3.2 *Tendon-to-Bone Insertion Dynamic Behavior*

The following sections present the application of the QPLM to the dynamically loaded tendon-to-bone insertion specimens.

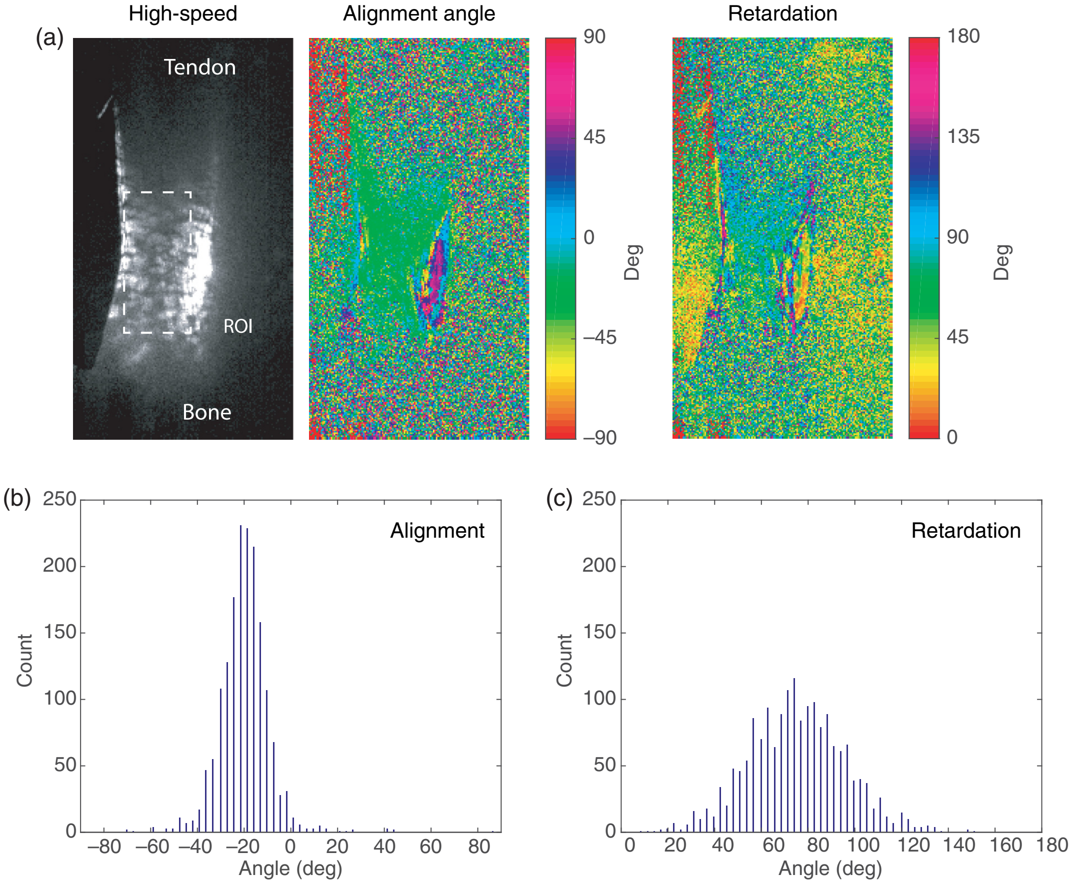

Fig. 6 (a) Selected light intensity image of the high-speed video of tendon-to-bone insertion sample under static tensile load and corresponding calculated alignment and retardation images. Tendon side is at top of image. Bone side is at bottom of image. Histogram of (b) alignment angle and (c) retardation angle distributions for ROI shown in (a).

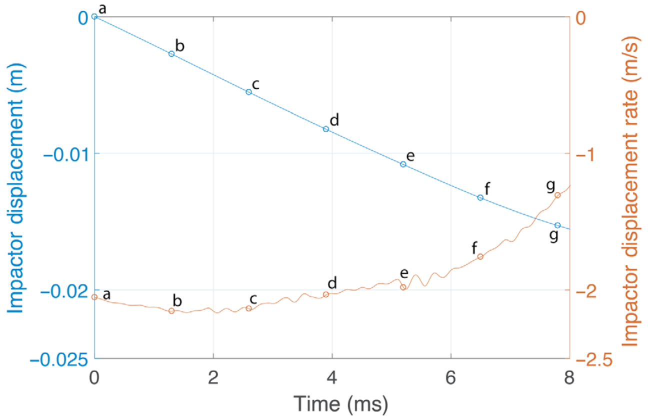

Fig. 7 Displacement and displacement rate of the impactor during loading of specimen 1 test.

Table 1 Time of initial failure for each tendon-bone insertion specimen tested.

Specimen #	Time at failure (ms)
1	7.8
2	6.2
3	N/A
4	6.5
5	5.7
6	9.4
7	6.0
8	5.5

We begin the discussion with the results of specimen 1, as it was the thinnest of all the tendon specimens tested. The displacement of the impactor during the impact event is shown in Fig. 7. The displacement rate calculated from this curve is also plotted in this figure. The impactor fell freely until it hit the lower crosshead, at $\sim t = 0$ ms. Once the impactor contacted the crosshead, it decelerated due to the loading of the tendon-to-bone insertion specimen. Initially, the deceleration was small (points b–e) as tissue-level stress does not occur in the fiber–fibril complex until the fiber-level crimp has been straightened.[5–7] As the fiber-level crimp is straightened, the tendon-to-bone insertion stiffness increases and the impactor decelerates faster (points f–g). Once the specimen begins to fail (for this specimen at point g), the impactor again begins to accelerate. The time at failure for all of the specimens tested is listed in Table 1.

The average light intensity of a pixel in the tendon-to-bone insertion region of specimen 1 is also plotted in Fig. 5. The high-speed camera imaging sensor gain was 8.0 and 1.0 for the dynamic and the static load tests, respectively. The static specimen had a larger thickness than the specimen for dynamic testing, therefore, the light intensity did not increase by a factor of 8.0. The increase in imaging sensor gain for the dynamic tests resulted in a larger offset and smaller wave amplitude. Due to the rapidly moving specimen, the fringe visibility is reduced, highlighting the importance of collecting several images per alignment angle and retardation map reconstruction.

Figure 8 shows selections from the high-speed video images for specimen 1, as well as reconstructed collagen fiber alignment angle and retardation maps at the same time steps. The bone region is visible as the lower third of each image and the tendon region is visible in the upper region of the image. The edge of the bone is clearly visible as the bone region is not transparent. The tendon-to-bone insertion region is the thinner region at the center of the images. The alignment angle and retardation maps at each time value are based on the 60 images ending at the time

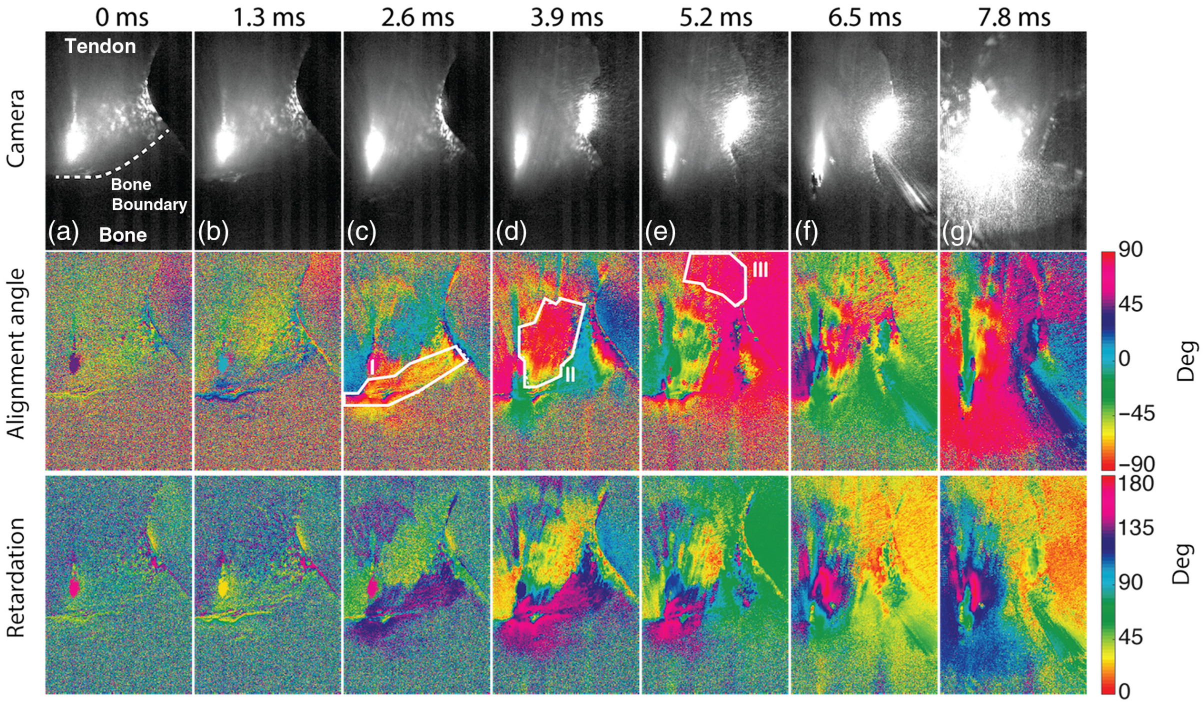

Fig. 8 Selected light intensity images of the high-speed video of tendon-to-bone insertion sample 1 under dynamic tensile load, and corresponding calculated alignment angle and retardation images. Tendon side is at top of image. Bone side is at bottom of image. Letters correspond to labeled times in Fig. 7.

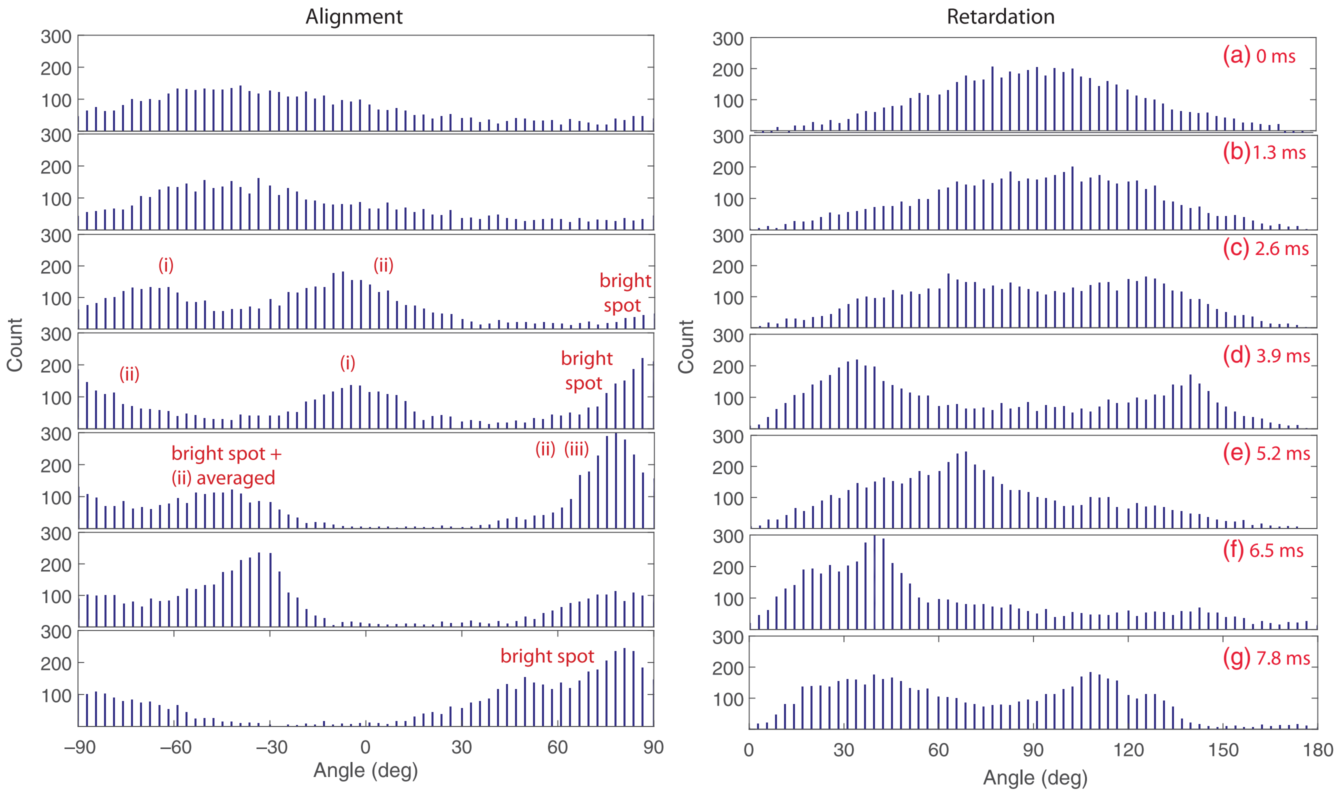

Fig. 9 Histogram of alignment angle and retardation images for specimen 1 from Fig. 8. Same ROI is used as for Fig. 6.

listed in this figure. The alignment angle represents the mean collagen fiber angle of orientation (relative to the horizontal axis) in the tissue at each pixel, whereas the retardation angle represents the strength of the fiber alignment.[7] Histograms of the alignment angle and retardation distributions are plotted in Fig. 9.

Just before the impact event began (shown as $t = 0$ ms), the video image shows clear transmission of the red light through the tendon-to-bone insertion sample. The transparency of the tendon-to-bone insertion is not uniform throughout the width of the sample, due to the challenges in slicing the sample uniformly. The bright region in the lower left-hand side of the image is a section of the field of view where there is no tissue material. The irregular shape of the tendon-to-bone insertion samples created such saturated regions in the video images for all of the samples, which could not be avoided if the entire tendon-to-bone insertion is to be imaged. As will be seen in the experimental results below, light leakage around the specimen boundaries did not create significant errors in the collagen fiber alignment angle and retardation maps, other than at the extreme edge of the specimens. At later time steps, starting at 3.9 ms, we see an additional bright region on the right-hand side of the sample, due to the tissue deforming, allowing a direct path for the light.

As the fiber alignment angle and retardation maps are calculated over a period of 60 images (6 ms), a relative delay appears between the video images and the two reconstructed maps. At the maximum displacement rate of 1.25 m/s, a location on the sample moves 7.5 mm over the course of the images. The actual displacement rate was lower than this value for most of the loading time, however, this spatial movement can create artifacts in some reconstructed maps.

Interpreting the retardation maps for some biological tissue specimens is challenging because the retardation depends on both the strength of the collagen fiber alignment and the thickness of the specimen. As it was difficult to maintain a uniform thickness for these specimens, we will only consider the uniformity of the retardation maps in this paper.

3.3 *Dynamic Collagen Fiber Realignment—Single Specimen*

The behavior of the tendon-to-bone insertion can be divided into several time intervals. A summary of the different collagen fiber realignment processes is listed in Table 2. In the first interval [images (a) and (b)], both the alignment angle and retardation maps show random noise, except for the bright spot where the light is not passing through the sample. The random noise indicates that the tissue is not birefringent and the measurements are likely dominated by scattering from the specimen. This is because the tissue-level stress does not occur in the fiber–fibril complex until the fiber-level crimp has been straightened, consistent with the low stiffness of the specimen observed from the impactor displacement rate curve in Fig. 7. Once the impact event begins, the level of alignment (as measured by the retardation map) increases, with measurable birefringence starting from $t = 1.4$ ms.

The alignment angle and retardation of the bright spot where the lightwaves pass around the specimen randomly vary throughout the loading, as shown by the histograms. Theoretically, these values should not change as the light path is not changing throughout the experiment. The raw intensity data for this region (and the other bright regions) was supersaturated since the camera settings were chosen to allow the

Table 2 Collagen fiber realignment processes in tendon-to-bone insertion and their time intervals for specimen 1.

Image	Time interval (ms)	Description of images	Description of behavior
a and b	0 to 1.3	Random alignment angle map throughout specimen	Collagen fibers coiled and not well aligned
c	1.4 to 2.8	Uniformity in alignment angle and retardation maps near bone end (region 1), weak alignment in middle of insertion region, other regions show low alignment	Collagen fibers near the bone end begin to align and rotate (region I)
d	2.9 to 4.3	Uniformity in alignment angle and retardation maps for bone end (region I) and midsection (region II), alignment angle maps in region I stabilized, in region II rotating	Collagen fibers in region I stabilize, collagen fibers in midsection of tendon-to-bone insertion align and rotate (region II)
e and f	4.4 to 7.0	Alignment angle and retardation maps relatively uniform across tendon-to-bone insertion	Collagen fibers throughout tendon-to-bone insertion begin to align in the same direction, beginning with tendon end (region III)
g	7.0 to 7.8	Alignment angle and retardation maps relatively uniform across tendon-to-bone insertion	Uniform deformation until failure of specimen

maximum graylevel range in the tissue regions of the image. As a result, the algorithm could not reconstruct the correct phase angle for these regions, however, this is not information related to the tissue behavior.

In the second interval [image (c)], we begin to see strong alignment near −75 deg in a region near the bone end of the tendon-to-bone insertion. This region is labeled as region I in Fig. 8. In this region, the collagen fibers are mostly type II and X collagen. The edge of the pure bone region is curved, therefore, as the bone end is displaced downward the collagen fibers must realign to follow the new local orientation of the pure bone edge. To show the transition more clearly, Fig. 10(a) shows four sequential alignment angle maps from this interval. The retardation histogram is beginning to divide into peaks for the specific regions, indicating that the previously isotropic region is rapidly increasing in anisotropy due to this uniform collagen fiber alignment. The tissue in the midsection of the tendon-to-bone insertion (region II) has also started to become more uniformly birefringent, however, the change in alignment angle is much smaller than that of region I.

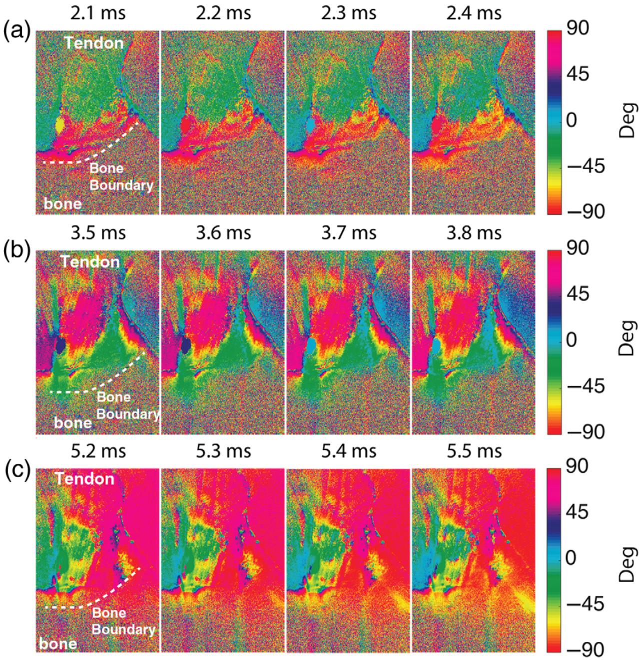

Fig. 10 Sequential alignment angle maps from interval (a) 2, (b) 3, and (c) 4.

In the third interval [image (d)], the tissue in region I has stabilized with a mean orientation close to −10 deg. In contrast, the tissue in region II, the midsection of the tendon-to-bone insertion, has significantly increased its fiber alignment. This fibrocartilage region is primarily type II and III collagen and has less mineral concentration, therefore, it is more flexible. Figure 10(b) shows the rapidly rotating fiber alignment angle for a sequence of images during this interval. The alignment angle starts near 60 deg and rotates to about −80 deg over this period (the alignment angle calculation wraps from 90 deg to −90 deg as these are both the vertical axis). This is a change of 40 deg over 0.3 ms. This angle is further from the vertical than expected and highlights the issues with time delays in high-speed QPLM imaging. For rapidly changing alignment angles, the mean angle calculated over the 0.6 ms of the images collected may vary from the final angle. Figure 10(b) shows a stronger uniformity of retardation in this region as well.

In the fourth interval [images (e) and (f)], the collagen fibers in the tissue near the tendon end of the tendon-to-bone insertion begin to align and rotate rapidly, creating the condition where the entire tendon-to-bone insertion rotates together. The collagen fibers in this region are primarily type I. The retardation maps show more uniformity across the entire tendon-to-bone insertion in this interval. A series of sequential alignment angle maps from this interval are shown in Fig. 10(c). The final alignment angle for most of the tendon-to-bone insertion just before failure was near 90 deg [image (e)].

The final failure of this specimen was at 7.8 ms [image (g)], through avulsion of the specimen at the tendon-to-bone insertion. A clear image of the start of the failure could not be seen in the raw camera intensity images for this specimen. The images at 7.8 ms were taken at the maximum displacement rate experienced by the specimen and clearly show the temporal bias in the alignment and retardation maps. In the camera intensity image, we observe that the specimen is clearly tearing with a large region of direct light from the laser arriving at the camera. However, the alignment and retardation maps appear relatively uniform across the tendon-to-bone insertion and do not show the random noise expected for the direct laser light. As the alignment angle and retardation maps are calculated over the 0.6 ms prior to the failure, the sudden change in intensity and random noise at the pixels in the direct laser path were measured only in the final phase angle images of 60 used in the calculation. The fast harmonic analysis method is able to mitigate the errors due such a rapid change in intensity, however, a significant temporal delay appears between the alignment angle and retardation maps and the camera images, which is displacement rate-dependent.

3.4 *Dynamic Collagen Fiber Realignment—Comparison Between Specimens*

Although the mean thickness of specimen 2 was slightly more than that of specimen 1, the difference was within the uncertainty of the thickness variation throughout a single specimen. The measured impactor displacement and displacement rate for specimen 2 are shown in Fig. 11 and are very close to the measurements for specimen 1. The collagen fiber alignment angle results for specimen 2, shown in Fig. 12, show the same five general intervals of behavior as listed in Table 2. For this specimen, the curved boundary of the bone was on the opposite side of the viewing area as compared to that of specimen 1. The three different regions highlighted in Fig. 8 are also highlighted in Fig 12. As can be seen in these images, the thickness of this specimen was considerably more uniform that of specimen 1. Slicing the thinnest specimen 1 produced more variability in the specimen thickness. The midsection region (II) of the tendon-to-bone insertion was also larger in specimen 2. The retardation and alignment angle maps showed larger areas of uniformity, presumably due to the more uniform thickness of the specimen. We still observe the rapid collagen fiber reorientation in the bond end of the specimen [(images (b) and (c)], followed by a reorientation of the midsection [images (d), (e), and (f)], and finally the complete tendon and tendon-to-bone insertion [image (g)]. A separation appeared in the specimen, visible as a bright vertical line, starting before loading of the specimen. The region to the right of this separation had approximately the same alignment angle and retardation behavior as the main region to the left of the separation, however, had a slightly higher noise level. This area of the sample was not included in the labeled regions I, II, and III. Again the failure was through avulsion of the specimen, the beginning of which can be seen in image (g).

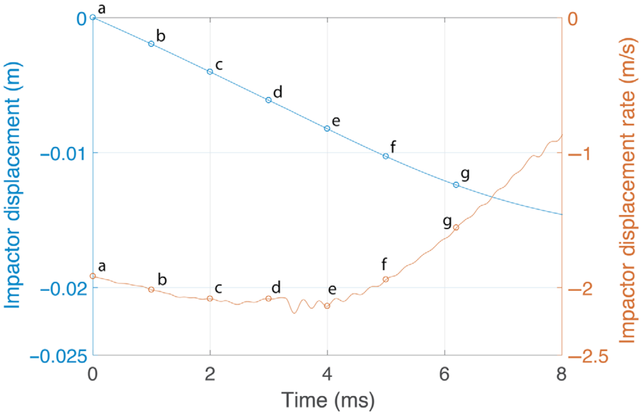

Fig. 11 Displacement and displacement rate of the impactor during loading of specimen 2 test.

As the thickness of specimen 2 was more uniform, the retardation maps from this specimen are more informative. In the mid-section of the specimen (region II) once the collagen fiber alignment is activated [image (c)], the phase retardation changes monotonically from 150 deg to 30 deg. The tensile loading increases the anisotropy in the tissue, and therefore, increases the retardation. However, the same tensile load also decreases the thickness of the tissue (due to the Poisson effect), which decreases the retardation of the material. Therefore, the sign of the retardation amplitude is difficult to interpret; however, the smooth change in retardation here is interpreted as a smooth increase in material anisotropy.

Raw video intensity images, alignment angle and retardation maps, collected at approximately the midpoint of the impact event

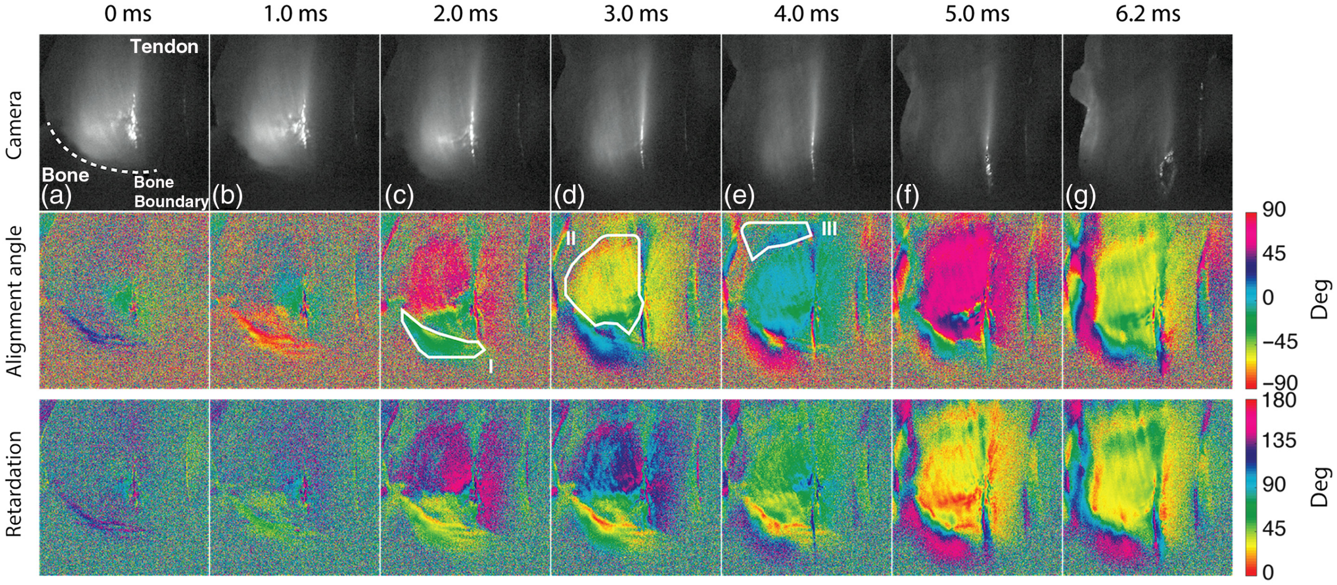

Fig. 12 Selected light intensity images of the high-speed video of tendon-to-bone insertion sample 2 under dynamic tensile load, and corresponding calculated alignment angle and retardation images. Tendon side is at top of image. Bone side is at bottom of image. Letters correspond to labeled times in Fig. 11.

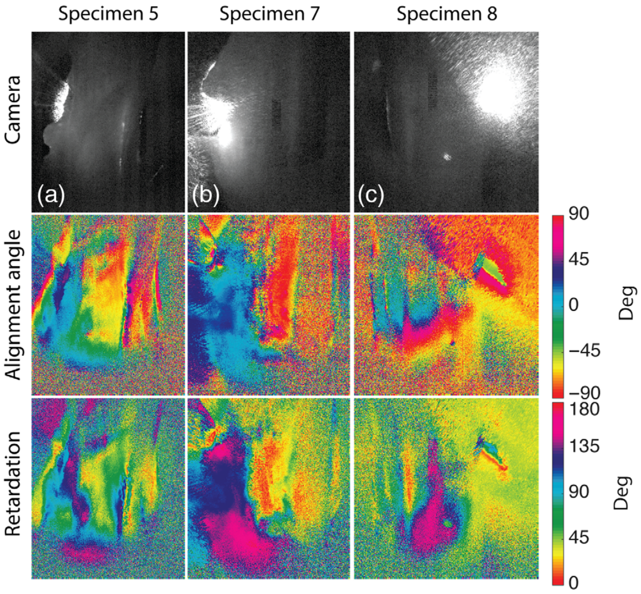

Fig. 13 Selected light intensity images of the high-speed video of tendon-to-bone insertion samples (a) 5, (b) 7, and (c) 8, and corresponding calculated alignment and retardation images. Tendon side is at top of image. Bone side is at bottom of image. All images collected at 4.5 ms after start of impact.

are shown for specimens 5, 7, and 8 in Fig. 13. We cannot compare the intensity of the light through each initial video image between specimens to determine their relative transparency, as this is dominated by the position of the QWP for the initial frame, which is random. However, the transparency of the specimens decreased with specimen thickness, as expected.

For the other specimens with small thicknesses, the same behaviors are still generally observed as for specimens 1 and 2. However, as the specimen thickness increased, the three regions become more difficult to distinguish from the alignment angle and retardation maps. This can be seen clearly by comparing the alignment angle and retardation images for the three specimens in Fig. 13. At the higher thicknesses, the reduced transparency of the specimen creates a high level of noise in the reconstruction maps. On the other hand, the thicker specimens are theoretically a more accurate representation of the tendon-to-bone insertion mechanical behavior in the original specimen, which had a thickness of 2 to 3 mm prior to slicing. Therefore, as we expected, there is a trade-off between the image quality and accuracy of the mechanical behavior data as a function of the specimen thickness.

4 Conclusions

The results of this paper demonstrate that slicing of tendon-to-bone insertion specimens, combined with high-speed QPLM is a viable experimental method to measure the nonlinear, transient behavior of tendon-to-bone insertion samples. We successfully loaded prepared digital tendon specimens under tensile loading at an average maximum displacement rate of 1.25 m/s. The specimen preparation (the extent of slicing of the tendon-to-bone insertion) played a role in the signal-to-noise ratio of the high-speed QPLM measurements, but did not significantly change the global mechanical behavior of the tendon-to-bone insertion or that of the local regions. The order of localized response within the tendon-to-bone insertion, and therefore, the mechanisms with which the tendon-to-bone insertion alleviates the high-stress rates induced, remained the same between samples. For the thicker specimens, the quality of the high-speed QPLM images was not sufficient to capture the localized behavior in the different regions of the tendon-to-bone insertion; however, the global response of the tendon-to-bone insertion remained the same.

The results also demonstrate that the tendon-to-bone insertion mitigates the potential impact of dynamic stress conditions through a sequence of localized deformations. First, the collagen fibers in the region at the bone end of the tendon-to-bone insertion realign to compensate for the relative movement of the curved bone interface. Once this initial, rapid realignment is completed, the collagen fibers in the midsection of the tendon-to-bone insertion realign to better map the new orientation in the bone end region to the orientation at the tendon end. Finally, the tendon-to-bone insertion globally realigns along with the joined tendon until failure of the tendon-to-bone insertion occurs through avulsion.

It should be noted that the order of the collagen fiber reorientation observed in these experiments may be a function of the fact that the impact load was applied to the bone end of the tendon-to-bone insertion, whereas in *in vivo* applications, the load may be applied to the tendon end. Although we have demonstrated the potential to use high-speed QPLM to measure the dynamic collagen fiber alignment, further experiments are needed to fully quantify the dynamic response of the tendon-to-bone insertion to the full range of typical loading encountered in events producing tendon-to-bone insertion injury.

Although these experiments were informative, the parameters of the QPLM system have also not yet been optimized. As mentioned previously, the QWP was rotated at 5000 rpm and the high-speed camera frame rate was 10,000 fps, therefore, the maximum number of images available (60) was used to calculate each alignment angle and retardation map. These rates were sufficient for the tests presented in this paper. For testing at lower displacement rates, the QWP rotation speed and camera frame rates could be reduced to minimize the light intensity required to transmit through the specimen, while still maintaining a reasonable error in the alignment angle and retardation calculations.[19] Although considering the specific rotation and frame rates, the potential temporal bias in images must also be considered. As seen in these experiments, the bias creates an apparent time lag between the alignment angle and retardation maps and the camera intensity images. For some applications, this time lag is the limiting factor in this measurement technique. However, as long as the rotation and frame rates are sufficient compared to the dynamics of the event, the time lag can be easily corrected if the specimen displacement rate as a function of time is measured.

Disclosures

The authors have no relevant financial interests in this article and no potential conflicts of interest to disclose.

Acknowledgments

We would like to thank National Science Foundation for financial support of this research (No. CMMI 1400018). K. Peters was also supported by the US National Science Foundation (while working at the Foundation). Any opinion, finding, conclusion, or recommendation expressed in this material are those of the authors and do not necessarily reflect the views of the National Science Foundation.

References

1. J. A. Weiss, J. C. Gardiner, and C. Bonifasi-Lista, "Ligament material behavior is nonlinear, viscoelastic and rate-independent under shear loading," *J. Biomech.* **35**(7), 943–950 (2002).
2. C. Bonifasi-Lista et al., "Viscoelastic properties of the human medial collateral ligament under longitudinal, transverse and shear loading," *J. Orthop. Res.* **23**(1), 67–76 (2005).
3. S. Thomopoulos et al., "Collagen fiber orientation at the tendon to bone insertion and its influence on stress concentrations," *J. Biomech.* **39**(10), 1842–1851 (2006).
4. D. A. Parry, "The molecular fibrillar structure of collagen and its relationship to the mechanical properties of connective tissue," *Biophys. Chem.* **29**(1–2), 195–209 (1988).
5. W. Goth et al., "Optical-based analysis of soft tissue structures," *Annu. Rev. Biomed. Eng.* **18**, 357–385 (2016).
6. B. Yang et al., "Collagen fiber orientation mapping with top layer discrimination using polarized light spatial frequency domain imaging (pSFDI) on native heart tissue," in *Biomedical Optics*, Optical Society of America, p. BM4B.5 (2014).
7. T. T. Tower and R. T. Tranquillo, "Alignment maps of tissues: II. Fast harmonic analysis for imaging," *Biophys. J.* **81**(5), 2964–2971 (2001).
8. T. T. Tower, M. R. Neidert, and R. T. Tranquillo, "Fiber alignment imaging during mechanical testing of soft tissues," *Ann. Biomed. Eng.* **30**(10), 1221–1233 (2002).
9. M. I. Danto and S. L.-Y. Woo, "The mechanical properties of skeletally mature rabbit anterior cruciate ligament and patellar tendon over a range of strain rates," *J. Orthop. Res.* **11**(1), 58–67 (1993).
10. N. Yoganandan et al., "Dynamic response of human cervical spine ligaments," *Spine* **14**(10), 1102–1110 (1989).
11. V. Shim, J. Liu, and V. Lee, "A technique for dynamic tensile testing of human cervical spine ligaments," *Exp. Mech.* **46**(1), 77–89 (2006).
12. M. M. Panjabi et al., "The mechanical properties of human alar and transverse ligaments at slow and fast extension rates," *Clin. Biomech.* **13**(2), 112–120 (1998).
13. P. C. Ivancic et al., "Dynamic mechanical properties of intact human cervical spine ligaments," *Spine J.* **7**(6), 659–665 (2007).
14. S. Chandrasekaran et al., "Composition and structure of porcine digital flexor tendon-bone insertion tissues," *J. Biomed. Mater. Res. A* **105**, 3050–3058 (2017).
15. K. P. Quinn and B. Winkelstein, "Vector correlation technique for pixel-wise detection of collagen fiber realignment during injurious tensile loading," *J. Biomed. Opt.* **14**(5), 054010 (2009).
16. K. P. Quinn et al., "Anomalous fiber alignment during tensile loading of the rat facet capsular ligament identifies mechanically induced damage and physiological dysfunction," *J. Biomech.* **43**(13), 1870–1875 (2010).
17. A. Harvey et al., "Functional imaging of tendon," *Ann. Br. Mach. Vision Assoc.* **2009**, 1–11 (2009).
18. K. P. Quinn and B. A. Winkelstein, "Altered collagen fiber kinematics define the onset of localized ligament damage during loading," *J. Appl. Physiol.* **105**(6), 1881–1888 (2008).
19. X. Wu et al., "High-speed polarized light microscopy for in-situ, dynamic measurements of birefringence properties," *Meas. Sci. Technol.* **29**(1), 015203 (2018).
20. T. York et al., "Real-time high-resolution measurement of collagen alignment in dynamically loaded soft tissue," *J. Biomed. Opt.* **19**(6), 066011 (2014).
21. V. Gruev, R. Perkins, and T. York, "CCD polarization imaging sensor with aluminum nanowire optical filters," *Opt. Express* **18**(18), 19087–19094 (2010).
22. T. T. Tower and R. T. Tranquillo, "Alignment maps of tissues: I. Microscopic elliptical polarimetry," *Biophys. J.* **81**(5), 2954–2963 (2001).

Xianyu Wu received his bachelor degree from the University of Electronic Science and Technology of China in 2011, and his MS and PhD degrees in mechanical engineering from the North Carolina State University in 2014 and 2018, respectively. He conducts research on high-speed imaging of biological materials.

Mark Pankow received his BS degree in mechanical engineering from California Polytechnic State University, San Luis Obispo, California, USA, in 2005, and his MS and PhD degrees in mechanical engineering from the University of Michigan in 2007 and 2010, respectively. He is the author of more than 50 journal papers and has written 3 book chapters. In 2012, he joined the faculty of the Department of Mechanical and Aerospace Engineering at North Carolina State University, where he conducts research on dynamic testing of materials.

Hsiao-Ying Shadow Huang received her MS and PhD degrees in mechanical engineering and materials science from the University of Pittsburgh. She is an associate professor of mechanical and aerospace engineering at NC State University. Prior joining NC State University in 2010, she was a postdoctoral associate at MIT. During her tenure at NC State University, she teaches and conducts research in the areas of mechanics of materials, nonequilibrium thermodynamics, continuum mechanics, and nonlinear elasticity. Her research programs are centered on understanding the mechanics of cardiovascular and musculoskeletal tissues. She was an NSF CAREER award recipient in 2016.

Kara Peters received her PhD in aerospace engineering from the University of Michigan in 1996. Until 2000, she was a researcher at the Ecole Polytechnique Fédérale de Lausanne, Laboratory of Applied Mechanics and Reliability, Switzerland. In 2000, she joined the Faculty of the Department of Mechanical and Aerospace Engineering at North Carolina State University, where she conducts research on optical fiber sensors, experimental mechanics, and imaging techniques. She is a fellow of SPIE.